J. Fluid Mech. (2005), *vol.* 524, *pp.* 99–120.
DOI: 10.1017/S002211200400182X Printed in the United Kingdom

Resonant Langmuir-circulation–internal-wave interaction. Part 2. Langmuir circulation instability

By G. P. CHINI[1] AND S. LEIBOVICH[2]

[1]Mechanical Engineering Department, University of New Hampshire, Durham, NH 03824, USA
[2]Sibley School of Mechanical and Aerospace Engineering, Cornell University, Ithaca, NY 14853, USA

(Received 11 August 2003 and in revised form 27 July 2004)

A long-wavelength weakly nonlinear analysis is used to investigate the possibility for resonant energy exchange between low-mode internal waves and counter-rotating roll vortices known as Langmuir circulation. The analysis is based on a two-layer ocean model in which the Langmuir circulation is confined to the upper layer and counter-propagating internal waves travel along the sharp thermocline normal to the axes of the vortices. An asymptotically consistent description of the slow-time behaviour is obtained by making a WKBJ approximation to treat the comparatively high-frequency internal-wave reflections identified in Part 1. When the vortices and waves are modelled as linearly neutral modes, the resulting dynamics take the form of nonlinear oscillations. The theory suggests that Langmuir cells may transiently lose stability to standing internal-wave disturbances whose nodes are aligned with the cell downwelling zones. An exact solution of the Langmuir-circulation–standing-wave interaction is used to gain insight into the nonlinear instability mechanism. As in Part 1, the modification of the linear internal-wave dynamics by the Craik–Leibovich 'vortex force' is found to be crucial to the interaction.

1. Introduction

Nonlinear interactions between waves and convection occur in a variety of flows ranging from free-surface Rayleigh–Marangoni–Bénard experiments (Colinet, Legros & Velarde 2001) to convectively coupled waves in the tropical atmosphere (Lindzen 2003). When the coupling is weak, amplitude equations can provide a useful tool for understanding the interaction mechanisms. The weakly nonlinear analysis presented here is motivated by a form of oceanic convection known as Langmuir circulation. Ranging in scale from a few metres to one kilometre (Thorpe 2004), Langmuir cells are wind-aligned counter-rotating roll vortices that arise as an instability of a wind-driven shear flow on which surface waves propagate (Craik & Leibovich 1976; Leibovich 1977, 1983). Langmuir circulation is thought to play a prominent role in upper-ocean dispersion and in the establishment and maintenance of wind-driven mixed layers. The large-eddy simulations (LES) of McWilliams, Sullivan & Moeng (1997) indicate that the largest vortices have a vertical scale commensurate with the depth of the near-surface mixed layer. This prompts the question: can Langmuir circulation interact with *in situ* internal waves propagating along the thermocline? Although observational evidence for this coupling is fragmentary, Thorpe (2004) argues that further investigation is warranted. His earlier theoretical study indicates that internal waves may twist and stretch the vortices, possibly contributing to their

observed variability (Thorpe 1997). Furthermore, the observations of Farmer, Vagle & Li (2001) and the LES of McWilliams *et al.* (1997) suggest that interactions between Langmuir circulation and the stratification at the base of the mixed layer may increase internal-wave activity within the thermocline.

In Part 1 (Chini & Leibovich 2003), we formulated a highly idealized mathematical model to investigate the possibility for resonant coupling between stationary Langmuir circulation of wavenumber $2k$ and counter-propagating internal waves of wavenumber k. Amplitude equations were derived by assuming that the wavelength of each mode is large compared to the depth of the mixed layer (i.e. $k \to 0$) and that the modal amplitudes are small ($O(k)$). The Langmuir circulation was found to mediate a conservative energy exchange between the internal waves over an $O(k^{-2})$ time scale but otherwise remain unaffected by the interaction. Here, we extend our analysis to longer times to study the possibility for Langmuir-circulation–internal-wave energy transfers. As in Part 1, a primary aim is to gain insight into the physics of the interaction.

Our asymptotic analysis is a blend of previous studies of (i) long-wavelength convection, (ii) 2:1 resonance phenomena and (iii) counter-propagating waves. Long-wavelength instabilities generally arise when near-constant- or zero-flux boundary conditions are applied at the upper and lower boundaries of the convection zone. Numerous authors have exploited the smallness of the critical wavenumber in such situations to derive asymptotically accurate long-wavelength amplitude equations, e.g. Busse & Riahi (1980), Chapman & Proctor (1980), Gertsberg & Sivashinsky (1981), Knobloch (1990) and Cox (1997) for Rayleigh–Bénard convection; Sivashinsky (1982) and Colinet *et al.* (2001) for surface-tension-driven convection; Sivashinsky (1983) for solidification of a binary alloy; Hefer & Pismen (1987) and Pismen (1988) for thermodiffusional convection; and Cox & Leibovich (1993, 1994, 1997) for Langmuir circulation. Unlike Cox & Leibovich, we do not treat spatial amplitude modulation; we do, however, account for the deformability of the thermocline. While several authors have investigated commensurate-scale interactions between long-wavelength deformational and cellular convection modes (Garcia-Ybarra, Castillo & Velarde 1987; Golovin, Nepomnyashchy & Pismen 1995; Colinet *et al.* 2001) and disparate-scale interactions between long-wavelength interfacial waves and short-wavelength convection cells (e.g. Pavithran & Redekopp 1994), our work differs both in the asymptotic scalings we employ and in our focus on a 2:1 spatial-resonance phenomenon.

The resonant reflection of propagating internal waves from stationary Langmuir cells predicted in Part 1 is somewhat akin to the Bragg reflection of surface waves from rippled sandbars (Mei 1985). A similar three-wave 2:1 resonant interaction also occurs in the rapidly rotating shallow-water equations: a stationary quasi-geostrophic mode of wavenumber $2k$ allows a passing inertio-gravity wave of wavenumber k to scatter into a counter-propagating wave without, itself, being affected by the gravity waves (Majda 2000). Employing a rigorous averaging procedure, Majda and collaborators demonstrate that even over longer time scales the quasi-geostrophic mode continues to evolve freely of the noisy sea of high-frequency inertio-gravity waves. In contrast, within the context of our idealized model, we show that Langmuir circulation can exchange energy with counter-propagating internal waves over sufficiently long (i.e. $O(k^{-3})$) time periods. For certain initial conditions, this energy exchange is manifested as a mode-switching behaviour, a rather robust outcome of 2:1 spatial resonances (see e.g. Proctor & Jones 1988; Johnson & Narayanan 1996; Colinet *et al.* 2001) which can be traced to a heteroclinic orbit in the reduced-order system.

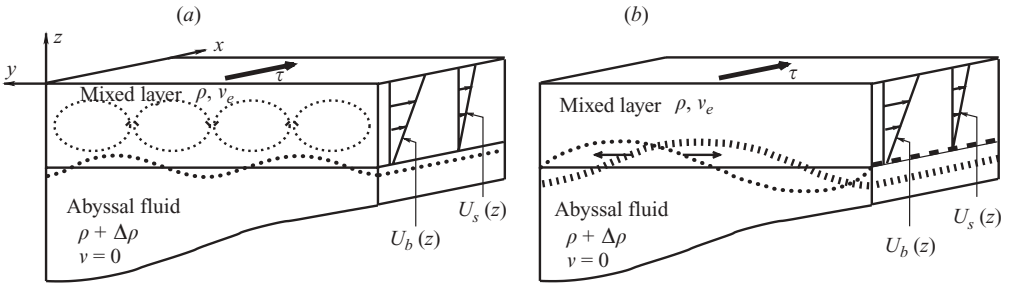

FIGURE 1. Two-layer schematic depicting (*a*) stationary Langmuir cells and (*b*) propagating internal waves. Note that the cells induce a static deformation of the thermocline.

The extension of our resonant interaction analysis to longer time scales requires care to ensure that an asymptotically consistent set of amplitude equations is obtained. As discussed by Knobloch & De Luca (1990), Knobloch & Gibbon (1991) and Pierce & Knobloch (1994), this complication arises in a number of reflection-symmetric systems supporting counter-propagating wave modes. In the case of capillary–gravity waves, for example, two coupled nonlinear-Schrödinger equations can be obtained for the $O(\epsilon)$ amplitudes of the counter-propagating waves, but these equations are strictly valid only when the group velocity $C_g = O(\epsilon)$, ensuring that all terms in the amplitude equations are of the same asymptotic order. Pierce & Knobloch (1994) demonstrate that a consistent set of amplitude equations valid for $O(1)$ group velocities can be derived by introducing two slow time scales and averaging over the 'faster' of these slow scales. The issue is not merely academic: the stability properties of the non-uniform and properly-averaged amplitude equations differ, i.e. the latter indicate that standing capillary–gravity waves are more stable to longitudinal perturbations than do the non-uniform equations. Physically, when $C_g = O(\epsilon)$, each wave moves slowly enough to 'sense' every fluctuation of the counter-propagating wave, leading to strong coupling. When $C_g = O(1)$, however, the waves 'see' each other only through their mean-square amplitudes; consequently, the coupling between the waves is much weaker. In our analysis, we follow Knobloch and co-workers by introducing an additional ($O(k^{-3})$) slow time variable and averaging over the original ($O(k^{-2})$) slow time scale.

The outline of the paper is as follows. For completeness, we first (in § 2) recall the problem formulation and key modelling assumptions developed in Part 1. We then extend our asymptotic analysis to longer time scales to study Langmuir-circulation–internal-wave energy exchanges (§ 3). The dynamics of the higher-order interaction equations are investigated in § 4, where a mode-switching nonlinear oscillation is identified. In § 5, we obtain an exact solution describing the nonlinear instability of Langmuir circulation to standing-internal-wave disturbances. This solution is used to gain insight into the physics of the instability mechanism. We conclude with a discussion of our key results (§ 6).

2. Problem formulation

Owing in part to the mixing accomplished by Langmuir circulation, the mean density distribution in the upper 10 to 100 m of the ocean is often nearly uniform. The density varies sharply at the base of this mixed layer, which is therefore the site of much internal wave activity. Motivated by these observations, we have formulated a semi-infinite two-layer ocean model (figure 1) to investigate the possibility for resonant

coupling between stationary Langmuir cells and counter-propagating internal (more properly, 'interfacial') waves (Part 1). We assume that the Langmuir circulation is maintained near marginal stability by the wind and surface waves and that the discrete stratification confines the vortices to the viscous upper ('mixed') layer of depth h. We restrict attention to downwind-invariant flows, i.e. to internal waves that propagate along the interface (the 'thermocline') normal to the wind-aligned axes of the vortices. Resonance is possible if a free internal wave, imposed via non-zero initial conditions, has a wavenumber k one-half that of the Langmuir circulation – the scenario considered both here and in Part 1. The surface-wave Stokes drift $U_s(z)$ is assumed to be aligned in the x-direction with the applied wind stress and, for analytical simplicity, taken to be a linear function of depth $(-z)$ that decays to zero at the base of the mixed layer. We have verified that a more realistic exponentially decaying profile yields no qualitative change in our key results. Since Coriolis effects are neglected, the wind-driven quasi-steady basic-state shear flow $U_b(z)$ is also aligned in the x-direction. Observations and numerical simulations (see e.g. figure 2 of McWilliams *et al.* 1997) indicate that the density jump across the thermocline confines not only the Langmuir circulation but also much of the small-scale turbulence – parameterized here with a constant eddy viscosity ν_e – to the mixed layer, causing wind-driven currents to be much faster above than below the thermocline. Consequently, we model the lower layer as an inviscid region. The wind stress applied at the sea surface $\tau = \rho u_*^2$, where ρ is the water density in the upper layer and u_* is the water friction velocity, is carried by weak but continual turbulent entrainment of lower-layer fluid into the mixed layer. The entrainment velocity w_e is small once the mixed layer has been established – on the order of a few metres per day under constant forcing conditions (Phillips 1977; McWilliams *et al.* 1997). As shown in Part 1, the critical Langmuir circulation wavenumber $k_{LC}^c \equiv 2k$ is $O(\alpha^{1/4})$ as $\alpha \equiv w_e h/\nu_e$ tends to zero. By exploiting this limit (following Cox & Leibovich 1993, 1994, 1997), we are able to make significant analytical progress and, in turn, to gain insight into the interaction mechanisms. One criticism of this approach, however, is that most observations and numerical simulations of strongly forced Langmuir circulation suggest that the dominant cells have an $O(1)$ rather than asymptotically large aspect ratio, making the link between our analysis and the dynamics of actual Langmuir circulation somewhat tenuous. Fortuitously, the small-k asymptotic analysis appears to correctly capture the linear dynamics of Langmuir circulation, as demonstrated by Cox (1997), and interfacial gravity waves (as we have verified) even for wavenumbers approaching unity, with relative errors in growth rates, phase speeds and critical wavenumbers less than 5%.

Although given in Part 1, the equations and boundary conditions governing perturbations to the quasi-steady horizontally uniform basic state are repeated here for completeness. Upper-layer perturbations satisfy the following non-dimensional equations:

$$\frac{\partial u}{\partial t} + v\frac{\partial u}{\partial y} + w\frac{\partial u}{\partial z} = -wR_* + \frac{1}{R_*}\left(\frac{\partial^2 u}{\partial y^2} + \frac{\partial^2 u}{\partial z^2}\right), \tag{2.1}$$

$$\frac{\partial v}{\partial t} + v\frac{\partial v}{\partial y} + w\frac{\partial v}{\partial z} = -\frac{\partial \pi}{\partial y} + S(1+z)\frac{\partial u}{\partial y} + \frac{1}{R_*}\left(\frac{\partial^2 v}{\partial y^2} + \frac{\partial^2 v}{\partial z^2}\right), \tag{2.2}$$

$$\frac{\partial w}{\partial t} + v\frac{\partial w}{\partial y} + w\frac{\partial w}{\partial z} = -\frac{\partial \pi}{\partial z} + S(1+z)\frac{\partial u}{\partial z} + \frac{1}{R_*}\left(\frac{\partial^2 w}{\partial y^2} + \frac{\partial^2 w}{\partial z^2}\right), \tag{2.3}$$

$$\frac{\partial v}{\partial y} + \frac{\partial w}{\partial z} = 0\,, \tag{2.4}$$

where velocities have been scaled by u_*, distances by h, time by h/u_* and densities by ρ. $R_* \equiv u_* h/\nu_e$ is an $O(1)$ rather than asymptotically large Reynolds number. Equations (2.1)–(2.3) are distinguished from the x-invariant instantaneous Navier–Stokes equations by the Craik–Leibovich (henceforth 'CL') vortex force terms arising in (2.2) and (2.3); these terms involve the non-dimensional Stokes drift $U_s(z) \equiv S(1+z)$ and account for the rectified effects of the surface waves, which are filtered in CL theory. In particular, (2.2) shows that vertical vorticity perturbations $\partial u/\partial y$ associated with downwind velocity anomalies feed back upon the cross-wind flow through the y-component of the CL vortex force. Given our assumptions, the lower-layer motion is irrotational and, hence, concisely described by introducing a velocity potential ϕ, where $\partial\phi/\partial y$ and $\partial\phi/\partial z$ are the lower-layer y- and z-velocity components. The non-dimensional free-surface and large-depth boundary conditions are given by

$$\frac{\partial u}{\partial z}(y,0,t) = \frac{\partial v}{\partial z}(y,0,t) = w(y,0,t) = 0, \tag{2.5}$$

and

$$\phi(y,z,t) \to 0 \quad \text{as} \quad z \to -\infty, \tag{2.6}$$

respectively, while the interfacial conditions at $z \equiv -1+\eta$ are

$$w = \frac{\partial \eta}{\partial t} + v\frac{\partial \eta}{\partial y}, \tag{2.7}$$

$$\frac{\partial \phi}{\partial z} = \frac{\partial \eta}{\partial t} + \frac{\partial \phi}{\partial y}\frac{\partial \eta}{\partial y}, \tag{2.8}$$

$$-(1+\gamma)\frac{\partial \phi}{\partial t} - \frac{(1+\gamma)}{2}|\nabla\phi|^2 = \pi + \gamma F\eta + \int_{-1}^{-1+\eta} S(1+z)\frac{\mathrm{d}\,U_b(z)}{\mathrm{d}z}\,\mathrm{d}z + \left[1+\left(\frac{\partial \eta}{\partial y}\right)^2\right]^{-1}\frac{2}{R_*}\left[-\frac{\partial w}{\partial z} + \frac{\partial \eta}{\partial y}\left(\frac{\partial v}{\partial z}+\frac{\partial w}{\partial y}\right) - \left(\frac{\partial \eta}{\partial y}\right)^2\frac{\partial v}{\partial y}\right], \tag{2.9}$$

$$\frac{\partial u}{\partial z} + \frac{\mathrm{d}U_b}{\mathrm{d}z} - \frac{\partial \eta}{\partial y}\frac{\partial u}{\partial y} = \alpha(u+U_b), \tag{2.10}$$

$$\left[1-\left(\frac{\partial \eta}{\partial y}\right)^2\right]\left(\frac{\partial v}{\partial z}+\frac{\partial w}{\partial y}\right) + 4\frac{\partial \eta}{\partial y}\frac{\partial w}{\partial z} = \alpha\left\{\left[v-(1+\gamma)\frac{\partial \phi}{\partial y}\right] + \frac{\partial \eta}{\partial y}\left[w-(1+\gamma)\frac{\partial \phi}{\partial z}\right]\right\}. \tag{2.11}$$

$\gamma \equiv \Delta\rho/\rho$ is the normalized density jump across the thermocline, and $F \equiv gh/u_*^2$ is the square of an inverse Froude number (where g is the gravitational acceleration). Finally, we note that $\mathrm{d}\hat{h}/\mathrm{d}t \equiv \alpha/R_* = O(k^4)$, where the mean non-dimensional mixed-layer depth $\hat{h} = O(1)$; since the longest interaction time scale we treat is $O(k^{-3})$, we can consistently neglect the implied mixed-layer deepening in our analysis (as in Part 1), justifying the use of a quasi-steady basic state $U_b(z) \equiv R_*[z+(\alpha+1)/\alpha]$.

3. Asymptotic analysis

We first obtain a non-uniform (i.e. not a rational asymptotic) set of higher-order resonant interaction equations, following the perturbation algorithm described in

Part 1, and then average the resulting ordinary differential equations to obtain a consistent set. This procedure is more transparent than averaging the partial differential equations and boundary conditions directly, and we have verified that it yields the same set of asymptotically consistent interaction equations.

3.1. *Non-uniform interaction equations*

We begin by expressing each dependent variable as the superposition of Langmuir-circulation, internal-wave and mean modes and expanding in powers of k, e.g.

$$\begin{aligned} u(y,z,t) = {} & [kU_{11}(\tau,T) + k^2u_{12}(z,\tau,T) + k^3u_{13}(z,\tau,T) + \ldots]\mathrm{e}^{\mathrm{i}2ky} \\ & + [kU_{21}(\tau,T) + k^2u_{22}(z,\tau,T) + k^3u_{23}(z,\tau,T) + \ldots]\mathrm{e}^{\mathrm{i}(ky-\omega t)} \\ & + [kU_{31}(\tau,T) + k^2u_{32}(z,\tau,T) + k^3u_{33}(z,\tau,T) + \ldots]\mathrm{e}^{\mathrm{i}(ky+\omega t)} \\ & + [k^2u_{42}(z,\tau,T) + k^3u_{43}(z,\tau,T) + \ldots] + \text{c.c.} + \text{h.o.t.}, \end{aligned} \tag{3.1}$$

where u is the downwind (x) current deviation from the basic-state shear flow, ω is the $O(k)$ internal-wave frequency, c.c. denotes complex conjugate and h.o.t. indicates higher-order terms. The first subscript indicates the mode type: 1 refers to Langmuir circulation, 2 and 3 to the positively and negatively propagating internal waves and 4 to horizontally uniform (i.e. mean) modes. The second subscript denotes the order in the small parameter k. U_{11}, U_{21} and U_{31} are the depth-averaged Langmuir-circulation and internal-wave downwind velocity perturbations. (In Part 1, these variables are denoted by U_{0100}, U_{0010} and U_{0001}.) Two slow time scales have been introduced, $\tau \equiv k^2t$ and $T \equiv k^3t$ (replacing T_{20} and T_{11}, and T_{30} and T_{21}, respectively, in Part 1), so that time-derivatives transform as $\partial/\partial t \mapsto \partial/\partial t + k^2\partial/\partial\tau + k^3\partial/\partial T$.

The perturbation algorithm for long-wavelength convection has been described elsewhere (e.g. Colinet *et al.* 2001) and adapted in Appendix A of Part 1 to account for propagating interfacial gravity waves; hence, only the central idea is repeated here. The $O(k)$ Langmuir-circulation (LC) downwind velocity u_{LC} and pressure π_{LC} are depth-independent, as expected for a thin fluid layer with nearly stress-free boundaries. For stationary, marginally stable cells, (2.2) then requires that the cross-wind velocity $v_{LC} = O(k^2)$, while the continuity equation, in turn, restricts Langmuir-cell upwelling and downwelling flows w_{LC} to be $O(k^3)$. Since the long-wavelength internal waves propagate with frequency $\omega = O(k)$, (2.2) shows that a balance is achieved among depth-independent $O(k)$ internal-wave (IW) pressure, cross-wind- and downwind-velocity perturbations (π_{IW}, v_{IW} and u_{IW}, respectively). Finally, the normal-stress condition (2.9) requires that the leading-order Langmuir-cell and internal-wave interfacial displacements, η_{LC} and η_{IW}, are both $O(k)$ to balance the pressure perturbations. As discussed in Part 1, advection of Langmuir-circulation vertical-vorticity perturbations $\partial u_{LC}/\partial y$ by cross-wind internal-wave currents v_{IW} results in a nonlinear transfer of the 'incident' wave energy to a counter-propagating wave, which itself ultimately attains an $O(k)$ amplitude. Given our scalings, this transfer is seen to occur over an $O(k^{-2})$ time scale. Here, we demonstrate that energy exchanges between the Langmuir circulation and internal waves occur over a longer, $O(k^{-3})$, time scale, essentially because weak vertical velocities, which are $O(k)$ relative to the cross-wind flows, play a crucial role in these exchanges – see § 5.

A sequence of linear problems is obtained at each order in k. Solvability conditions must be imposed because the linear operator has a zero eigenvalue: at $O(k)$, the leading-order problem for the Langmuir circulation reduces to $\partial^2 u_{LC}/\partial z^2 = 0$, subject to $\partial u_{LC}/\partial z = 0$ at $z = 0, -1$, which has the non-trivial solution $u_{LC} = kU_{11}(\tau,T)\exp(\mathrm{i}2ky) + \text{c.c.}$ Non-trivial solvability conditions determine

the Langmuir-circulation growth rate, the internal-wave phase speed and the nonlinear interaction coefficients.

After modifying the perturbation algorithm to account for the mean modes and restoring the original time variable, we obtain the following higher-order set of resonant interaction equations:

$$\frac{\mathrm{d}E}{\mathrm{d}t} = k^3\hat{\sigma}\,E + k^2 e_{nr1} AB + \mathrm{i}k e_{n_A}[|A|^2 - |B|^2]E, \tag{3.2}$$

$$\frac{\mathrm{d}A}{\mathrm{d}t} = [k^3 a_{lr1} + \mathrm{i}(k^2 a_{li0} + k^3 a_{li1})]A + [k^2 a_{nr1} + \mathrm{i}(k a_{ni0} + k^2 a_{ni1})]EB^* + \mathrm{i}k[a_{n_A}|A|^2 + a_{n_B}|B|^2 + a_{n_E}|E|^2]A, \tag{3.3}$$

$$\frac{\mathrm{d}B}{\mathrm{d}t} = [k^3 b_{lr1} - \mathrm{i}(k^2 a_{li0} + k^3 a_{li1})]B + [k^2 a_{nr1} - \mathrm{i}(k a_{ni0} + k^2 a_{ni1})]EA^* - \mathrm{i}k[a_{n_A}|B|^2 + a_{n_B}|A|^2 + a_{n_E}|E|^2]B. \tag{3.4}$$

In (3.2)–(3.4), asterisks denote complex conjugation, and we have made the replacements $kU_{11} \equiv E$, $kU_{21} \equiv A$ and $kU_{31} \equiv B$ so that the (small) modal amplitudes are given by E, A and B. In (3.2), we have used the result from Part 1 that $\partial U_{11}/\partial\tau = 0$.

If the near marginal-stability relationship $R_*^3 S/120 = 1 + O(k^2)$ holds (see Part 1), the linear growth rate of the cells $\sigma \equiv k^3\hat{\sigma}$ is formally $O(k^4)$, implying that the first term on the right-hand-side of (3.2) is fifth order in the combined small parameters. We retain this term to include the possibility for modelling supercritical Langmuir circulation (which, for consistency, formally requires $\hat{\sigma} = O(1)$ so that $R_*^3 S/120 = 1 + O(k)$). Similarly, to keep the formulation general, we have included in an *ad hoc* fashion a linear growth/damping coefficient for each internal wave, a_{lr1} and b_{lr1}. (Recall that we have set the $O(k^2)$ damping coefficient, $a_{lr} \mapsto a_{lr0}$ in the notation of this article, to zero since observed internal-wave damping rates are much less than that predicted by this term.) At leading order, the internal-wave phase speed $c \equiv \omega/k = [\gamma F - R_* S/4]^{1/2}$, where we restrict $R_*^2 \gamma F > 30$. At higher-order, dispersive corrections arise:

$$a_{li0} = \frac{(R_*^2\gamma F - 30)^{1/2}}{2R_*}(1+\gamma), \tag{3.5}$$

$$a_{li1} = \frac{1}{R_*}\left[\frac{31}{336} - \frac{\gamma}{4} - \frac{\gamma^2}{8}\right](R_*^2\gamma F - 30)^{1/2} - \frac{2(1+\gamma)}{R_*} - \frac{930}{336R_*(R_*^2\gamma F - 30)^{1/2}}. \tag{3.6}$$

The imaginary interaction coefficients a_{ni0} ('a_{ni}' in the notation of Part 1) and a_{ni1} account for conservative energy exchanges between the counter-propagating internal waves, mediated by the Langmuir circulation. These coefficients are given by

$$a_{ni0} = -\frac{90}{R_*^4\gamma F}\left[\frac{R_*^2\gamma F - 60}{(R_*^2\gamma F - 30)^{1/2}}\right], \tag{3.7}$$

$$a_{ni1} = \frac{15(1+\gamma)}{R_*^4\gamma F}\left[\frac{R_*^2\gamma F - 120}{(R_*^2\gamma F - 30)^{1/2}}\right]. \tag{3.8}$$

The presence of non-zero real quadratic interaction coefficients

$$e_{nr1} = \frac{2}{R_*^2}\left[\frac{13R_*^2\gamma F - 180}{R_*^2\gamma F - 30}\right] \tag{3.9}$$

and

$$a_{nr1} = -\frac{450}{R_*^4 \gamma F}\left[\frac{R_*^2 \gamma F - 22}{R_*^2 \gamma F - 30}\right] \tag{3.10}$$

implies that, over the T time scale, the amplitude of the Langmuir circulation is altered by the interaction between the counter-propagating waves.

Finally, the coefficients of the cubic nonlinear terms arise from the interaction of the mean modes with the fundamental Langmuir-circulation or internal-wave modes. These coefficients are purely imaginary and, thus, account for modulations in the phases of the complex amplitudes (E, A and B) due to mixed-mode and self interactions. Specifically,

$$e_{n_A} = -\frac{4}{R_*^5 \gamma F}\left[\frac{162000 + 105 R_*^4 (\gamma F)^2 - 2700 \gamma F R_*^2 - 2 R_*^6 (\gamma F)^3}{(R_*^2 \gamma F - 30)^{3/2}}\right], \tag{3.11}$$

$$a_{n_A} = -\frac{240}{R_*^5 \gamma F}\left[\frac{R_*^2 \gamma F - 120}{(R_*^2 \gamma F - 30)^{1/2}}\right], \tag{3.12}$$

$$a_{n_B} = \frac{2}{R_*^5 \gamma F}\left[\frac{R_*^4 (\gamma F)^2 + 25200 + 180 \gamma F R_*^2}{(R_*^2 \gamma F - 30)^{1/2}}\right], \tag{3.13}$$

$$a_{n_E} = \frac{450}{R_*^9 (\gamma F)^3}\left[\frac{115200 \gamma F R_*^2 - 1680 R_*^4 (\gamma F)^2 + R_*^6 (\gamma F)^3 - 1728000}{(R_*^2 \gamma F - 30)^{3/2}}\right]. \tag{3.14}$$

The calculations were carried out by hand to $O(k^3)$ and checked using the symbolic algebra program given in Appendix B of Chini (1999). This program was also used to compute the $O(k^4)$ Langmuir circulation growth rate, which was shown in Part 1 to agree with the result of Cox & Leibovich (1993) in the rigid-thermocline limit. The higher-order perturbation calculations are unwieldy, and a second (independent) symbolic algebra routine was written to extend the nonlinear calculation to $O(k^4)$, yielding the coefficients reported above. We have verified that the new computer program reproduces all coefficients previously obtained by hand and with our first symbolic algebra program.

3.2. *Consistent equations via averaging*

Equations (3.2)–(3.4) contain terms which are formally of different asymptotic order; e.g. (3.3) includes nonlinear terms which are cubic and quartic in the products of the small amplitudes and small wavenumber. These amplitude equations should be viewed with caution, since they admit qualitatively different (actually, more complex) dynamics than do the consistent equations derived here.

Following Knobloch & De Luca (1990), we implicitly average over the $O(k^{-2})$ time scale to obtain amplitude equations that are asymptotically consistent for $t = O(k^{-3})$. It is convenient to first remove the linear phase-speed corrections in (3.3) and (3.4) by introducing the transformations $\tilde{A} \equiv A\exp[-\mathrm{i}(k^2 a_{li0} + k^3 a_{li1})t]$ and $\tilde{B} \equiv B\exp[\mathrm{i}(k^2 a_{li0} + k^3 a_{li1})t]$. The transformed equations are formally identical to (3.2)–(3.4) with A and B replaced by $\tilde{A}$ and $\tilde{B}$ and the a_{li0} and a_{li1} terms set to zero; for brevity, we henceforth drop the tildes. Next, we re-introduce the slow time scales $\tau \equiv k^2 t$ and $T \equiv k^3 t$, so that time-derivatives transform as $\mathrm{d}/\mathrm{d}t = k^2 \partial/\partial\tau + k^3 \partial/\partial T$,

and re-expand the amplitudes as asymptotic series in ascending powers of k:

$$E = kE_0(\tau, T) + k^2 E_1(\tau, T) + \ldots, \tag{3.15}$$

$$A = kA_0(\tau, T) + k^2 A_1(\tau, T) + \ldots, \tag{3.16}$$

$$B = kB_0(\tau, T) + k^2 B_1(\tau, T) + \ldots. \tag{3.17}$$

Substituting into the transformed versions of (3.2)–(3.4), we obtain at $O(k^3)$

$$\frac{\partial E_0}{\partial \tau} = 0, \tag{3.18}$$

$$\frac{\partial A_0}{\partial \tau} - \mathrm{i}a_{ni0}E_0B_0^* = 0, \tag{3.19}$$

$$\frac{\partial B_0}{\partial \tau} + \mathrm{i}a_{ni0}E_0A_0^* = 0. \tag{3.20}$$

From (3.18), we find that $E_0 = E_0(T)$; thus, (3.19) and (3.20) can be combined into a single second-order harmonic-oscillator equation with a slowly varying frequency. Making a WKBJ approximation (see e.g. Hinch 1991), we obtain

$$A_0(\tau, T) = A_+(T)\,\mathrm{e}^{\mathrm{i}\theta(\tau)} + A_-(T)\mathrm{e}^{-\mathrm{i}\theta(\tau)}, \tag{3.21}$$

$$B_0(\tau, T) = B_+(T)\,\mathrm{e}^{\mathrm{i}\theta(\tau)} + B_-(T)\mathrm{e}^{-\mathrm{i}\theta(\tau)}, \tag{3.22}$$

where $B_+ = -A_-^* E_0/|E_0|$, $B_- = A_+^* E_0/|E_0|$ and $\theta(\tau) \equiv k^{-1}\Theta(T)$, so that

$$\frac{\mathrm{d}\theta}{\mathrm{d}\tau}(\tau) = \frac{\mathrm{d}\Theta}{\mathrm{d}T}(T) = a_{ni0}|E_0(T)|. \tag{3.23}$$

Note that $\tau_P \equiv 2\pi/(|a_{ni0}||E_0|)$ is the slowly varying period of the τ-scale internal-wave reflections.

Extending the calculation to $O(k^4)$, we obtain the following set of equations:

$$\frac{\partial E_1}{\partial \tau} = \hat{\sigma}E_0 + e_{nr1}A_0B_0 + \mathrm{i}e_{n_A}[|A_0|^2 - |B_0|^2]E_0 - \frac{\mathrm{d}E_0}{\mathrm{d}T}, \tag{3.24}$$

$$\begin{aligned}\frac{\partial A_1}{\partial \tau} - \mathrm{i}a_{ni0}E_0B_1^* = {} & a_{lr1}A_0 - \frac{\partial A_0}{\partial T} + \mathrm{i}a_{ni1}E_0B_0^* + \mathrm{i}a_{ni0}E_1B_0^* + a_{nr1}E_0B_0^* \\ & + \mathrm{i}\left[a_{n_A}|A_0|^2 + a_{n_B}|B_0|^2 + a_{n_E}|E_0|^2\right]A_0,\end{aligned} \tag{3.25}$$

$$\begin{aligned}\frac{\partial B_1}{\partial \tau} + \mathrm{i}a_{ni0}E_0A_1^* = {} & b_{lr1}B_0 - \frac{\partial B_0}{\partial T} - \mathrm{i}a_{ni1}E_0A_0^* - \mathrm{i}a_{ni0}E_1A_0^* + a_{nr1}E_0A_0^* \\ & - \mathrm{i}\left[a_{n_A}|B_0|^2 + a_{n_B}|A_0|^2 + a_{n_E}|E_0|^2\right]B_0.\end{aligned} \tag{3.26}$$

Substituting (3.21) and (3.22) into (3.24) yields

$$\begin{aligned}\frac{\partial E_1}{\partial \tau} = {} & \hat{\sigma}E_0 + e_{nr1}[A_+B_+\mathrm{e}^{\mathrm{i}2\theta} + A_-B_-\mathrm{e}^{-\mathrm{i}2\theta} + (A_+B_- + A_-B_+)] - \frac{\mathrm{d}E_0}{\mathrm{d}T} \\ & + \mathrm{i}2e_{n_A}[A_+A_-^*\mathrm{e}^{\mathrm{i}2\theta} + A_+^*A_-\mathrm{e}^{-\mathrm{i}2\theta}]\,E_0.\end{aligned} \tag{3.27}$$

Since E_0, A_+ and A_- are independent of τ, E_1 will grow linearly with τ and, hence, (3.15) will not be uniformly asymptotic when $\tau = O(k^{-1})$ – that is, over the T-scale – unless the following secularity condition is satisfied:

$$\frac{\mathrm{d}E_0}{\mathrm{d}T} = \hat{\sigma}E_0 + e_{nr1}\frac{E_0}{|E_0|}[|A_+|^2 - |A_-|^2]. \tag{3.28}$$

Using (3.28), and noting that $\int \mathrm{e}^{\mathrm{i}2\theta(\tau)}\,\mathrm{d}\tau = F(T) + \mathrm{e}^{\mathrm{i}2\theta(\tau)}/(\mathrm{i}2a_{ni0}|E_0(T)|)$, where $F(T)$ is a function of integration and (3.23) has been used, integration of (3.27) yields $E_1(\tau, T) = E_{1_+}\mathrm{e}^{\mathrm{i}2\theta} + E_{1_-}\mathrm{e}^{-\mathrm{i}2\theta} + \langle E_1\rangle(T)$, where

$$E_{1_+} \equiv \left[\mathrm{i}\frac{e_{nr1}}{2a_{ni0}}\frac{E_0}{|E_0|^2} + \frac{e_{n_A}}{a_{ni0}}\frac{E_0}{|E_0|}\right] A_+A_-^*,\ E_{1_-} \equiv \left[\mathrm{i}\frac{e_{nr1}}{2a_{ni0}}\frac{E_0}{|E_0|^2} - \frac{e_{n_A}}{a_{ni0}}\frac{E_0}{|E_0|}\right] A_+^*A_-$$

and $\langle E_1\rangle(T)$ is the (running) average of $E_1(\tau, T)$ over τ_P. To determine the dynamics on the T-scale, we extend our normalization condition from Part 1 by requiring the time-average of the (depth-averaged) Langmuir circulation amplitude to satisfy

$$\langle E(\tau, T)\rangle \equiv k\langle E_0\rangle(T), \tag{3.29}$$

implying $\langle E_1\rangle(T) = 0$. The homogeneous solutions to (3.25) and (3.26) are analogous to (3.21) and (3.22). Secularity conditions arise because the inhomogeneous terms on the right-hand sides of (3.25) and (3.26) include terms proportional to $\mathrm{e}^{\mathrm{i}\theta(\tau)}$ and $\mathrm{e}^{-\mathrm{i}\theta(\tau)}$. Removal of these terms requires

$$\begin{aligned}\frac{\mathrm{d}A_+}{\mathrm{d}T} &= \Lambda A_+ + \mathrm{i}\,a_{ni1}|E_0|\,A_+ + \frac{e_{nr1}}{2}\frac{|A_-|^2}{|E_0|}\,A_+ + a_{nr1}|E_0|\,A_+ \\ &\quad + \mathrm{i}\left(2a_{n_A} - e_{n_A}\right)|A_-|^2A_+ + \mathrm{i}\left(a_{n_A} + a_{n_B}\right)|A_+|^2A_+ + \mathrm{i}a_{n_E}|E_0|^2A_+, \end{aligned}\tag{3.30}$$

$$\begin{aligned}\frac{\mathrm{d}A_-}{\mathrm{d}T} &= \Lambda A_- - \mathrm{i}\,a_{ni1}|E_0|\,A_- - \frac{e_{nr1}}{2}\frac{|A_+|^2}{|E_0|}\,A_- - a_{nr1}|E_0|\,A_- \\ &\quad + \mathrm{i}\left(2a_{n_A} - e_{n_A}\right)|A_+|^2A_- + \mathrm{i}\left(a_{n_A} + a_{n_B}\right)|A_-|^2A_- + \mathrm{i}a_{n_E}|E_0|^2A_-, \end{aligned}\tag{3.31}$$

where $\Lambda \equiv (a_{lr1} + b_{lr1})/2$. Equations (3.28), (3.30) and (3.31) govern the dynamics of the resonant triad over a time scale long compared to that over which the internal-wave reflections occur. Unlike (3.2)–(3.4), these equations are consistent in that they only contain terms of the same asymptotic order in the combined small parameters (i.e. amplitudes and wavenumber).

4. Interaction dynamics

In this section, we investigate the dynamics of (3.28), (3.30) and (3.31). A simplification can be achieved by converting to a magnitude–phase representation, i.e. $E = |E|\mathrm{e}^{\mathrm{i}\Phi}$, $A_+ = |A_+|\mathrm{e}^{\mathrm{i}\Phi_+}$ and $A_- = |A_-|\mathrm{e}^{\mathrm{i}\Phi_-}$, where henceforth we take A_+ and A_- to be $O(k)$, as is E (see (3.15)). Upon restoring the original time variable, we obtain

$$\frac{\mathrm{d}|E|}{\mathrm{d}t} = \sigma|E| + e_{nr}[|A_+|^2 - |A_-|^2], \tag{4.1}$$

$$\frac{\mathrm{d}|A_+|}{\mathrm{d}t} = \lambda|A_+| + \frac{e_{nr}}{2}\frac{|A_-|^2}{|E|}\,|A_+| + a_{nr}|E|\,|A_+|, \tag{4.2}$$

$$\frac{\mathrm{d}|A_-|}{\mathrm{d}t} = \lambda|A_-| - \frac{e_{nr}}{2}\frac{|A_+|^2}{|E|}\,|A_-| - a_{nr}|E|\,|A_-|, \tag{4.3}$$

where $e_{nr} = k^2e_{nr1}$, $a_{nr} = k^2a_{nr1}$ and $\lambda = k^3\Lambda$, and

$$|E|\frac{\mathrm{d}\Phi}{\mathrm{d}t} = 0, \tag{4.4}$$

$$\begin{aligned}|A_+|\frac{\mathrm{d}\Phi_+}{\mathrm{d}t} &= k^2a_{ni1}\,|E|\,|A_+| + k\left(a_{n_A} + a_{n_B}\right)|A_+|^3 \\ &\quad + k\left(2a_{n_A} - e_{n_A}\right)|A_-|^2|A_+| + ka_{n_E}|E|^2|A_+|, \end{aligned}\tag{4.5}$$

$$|A_-|\frac{\mathrm{d}\Phi_-}{\mathrm{d}t} = -k^2 a_{ni1}|E||A_-| + k\left(a_{n_A}+a_{n_B}\right)|A_-|^3 + k\left(2a_{n_A}-e_{n_A}\right)|A_+|^2|A_-| + k a_{n_E}|E|^2|A_-|. \tag{4.6}$$

Thus, the magnitudes of the complex amplitudes evolve independently of the phases. From (4.4), we observe that the phase of the Langmuir circulation is not affected by the interaction, unless the amplitude of the cellular motion instantaneously reaches zero. As we demonstrate subsequently, $\mathrm{d}E/\mathrm{d}t$ remains finite and continuous at such an instant, implying that the only permissible phase shift is 180°; this phase shift can be achieved smoothly by a reversal in the orientation of the cellular motion. (We return to this point in § 5). Thus, without loss of generality, we may take E to be real, since this simply amounts to fixing the origin of our coordinate system. A further simplification can be realized by defining $\Sigma \equiv |E|$, $\Gamma \equiv |A_+|^2 + |A_-|^2$ and $\chi \equiv |A_+|^2 - |A_-|^2$, in terms of which (4.1)–(4.3) become

$$\frac{\mathrm{d}\Sigma}{\mathrm{d}\mathscr{T}} = \sigma_R \Sigma + \chi, \tag{4.7}$$

$$\frac{\mathrm{d}\chi}{\mathrm{d}\mathscr{T}} = \frac{\Gamma^2 - \chi^2}{2\Sigma} - 2r\,\Sigma\,\Gamma + 2\lambda_R\,\chi, \tag{4.8}$$

$$\frac{\mathrm{d}}{\mathrm{d}\mathscr{T}}[\Gamma + r\Sigma^2] = 2\lambda_R\,\Gamma + 2r\sigma_R\,\Sigma^2, \tag{4.9}$$

where $\mathscr{T} \equiv e_{nr}t$, $r \equiv (-a_{nr})/e_{nr} > 0$, $\sigma_R \equiv \sigma/e_{nr}$ and $\lambda_R \equiv \lambda/e_{nr}$.

Henceforth, we restrict attention to neutral Langmuir circulation ($\sigma_R = 0$) and undamped internal waves ($\lambda_R = 0$); see Part 1 for a discussion of our modelling rationale. Given this restriction, (4.9) can be immediately integrated, yielding

$$\Gamma + r\,\Sigma^2 = C, \tag{4.10}$$

where C is a positive constant determined by the initial conditions, and permitting (4.7) and (4.8) to be expressed as

$$\frac{\mathrm{d}\Sigma}{\mathrm{d}\mathscr{T}} = \chi, \tag{4.11}$$

$$\Sigma\frac{\mathrm{d}\chi}{\mathrm{d}\mathscr{T}} = \frac{5}{2}r^2\,\Sigma^4 - 3Cr\,\Sigma^2 + \frac{C^2-\chi^2}{2}. \tag{4.12}$$

Equations (4.11) and (4.12) can be combined into a single equation for $\chi = \chi(\Sigma(\mathscr{T}))$, which has the solution $\chi^2 = (C - r\Sigma^2)^2 - \kappa\Sigma^{-1} = \Gamma^2 - \kappa\Sigma^{-1}$, where κ is a positive constant. Using this solution, (4.11) can be reduced to a quadrature and $|A_+(\mathscr{T})|$ and $|A_-(\mathscr{T})|$ can then be determined. Although these solutions can be expressed in terms of 'hyper-elliptic' functions, examination of the χ–E phase portrait, shown in figure 2, proves more enlightening. There are fixed points at $[0, \pm(C/r)^{1/2}]$ and $[0, \pm(C/5r)^{1/2}]$, the former corresponding to saddle points and the latter to centres. Physically, the centres represent the extension of the 'pure' internal-wave reflection solution obtained in Part 1 to the T time scale: the Langmuir circulation amplitude remains steady ($|E| = E_c$, say), while the internal-wave amplitudes vary harmonically in time, 90° out-of-phase, with amplitude $[2(C - rE_c^2)]^{1/2}$ and modified frequency $k|a_{ni0} + ka_{ni1}|E_c$. The saddle-node solutions correspond to steady Langmuir circulation in the absence of internal waves; clearly, these (phase-shifted) solutions are unstable. They are connected by a pair of singular heteroclinic trajectories which intersect along the χ-axis between $\chi = -C$ and $\chi = C$. Equation (4.12) implies $\mathrm{d}\chi/\mathrm{d}\mathscr{T} \to \infty$ in that region, i.e. χ changes discontinuously from $-C$ to C, permitting $\mathrm{d}E/\mathrm{d}\mathscr{T}$ to remain finite and

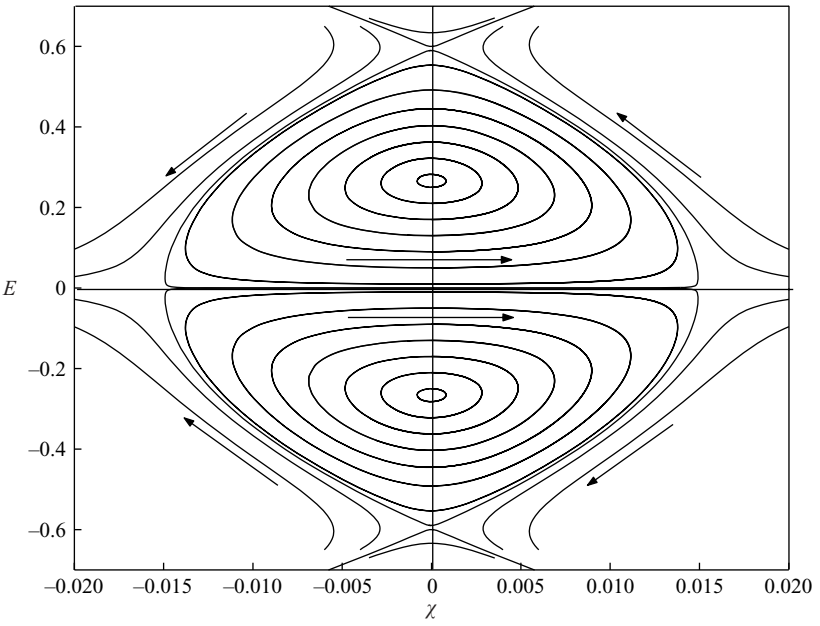

FIGURE 2. The χ–E phase portrait, with $\sigma_R = \lambda_R = 0$, $k = 0.5$, $R_* = 2$, $\gamma F = 100$, $r = 0.042$ and $C = 0.015$. A pair of heteroclinic orbits connects the saddle points at $[0, \pm(C/r)^{1/2}]$. Physically admissible solutions are confined to the closed orbits around the centres at $[0, \pm(C/5r)^{1/2}]$, which correspond to nonlinear oscillations in the Langmuir-circulation and internal-wave amplitudes, and to the heteroclinic connections, which correspond to a Langmuir-circulation–standing-wave interaction.

continuous as E passes through zero. For example, for the heteroclinic connection emanating from the saddle point at $\chi = (C/r)^{1/2}$, $\mathrm{d}E/\mathrm{d}\mathscr{T} = \chi = -C$, as $E \to 0^+$ and $\chi < 0$, while $\mathrm{d}(-E)/\mathrm{d}\mathscr{T} = \chi = C$, as $E \to 0^-$ and $\chi > 0$. Similar reasoning applies to the other heteroclinic orbit, except that $\mathrm{d}E/\mathrm{d}\mathscr{T} = C$ as E passes through zero along that trajectory. In § 5, we obtain closed-form solutions for the heteroclinic orbits and show that they correspond to a Langmuir-circulation–standing-internal-wave interaction; the singular behaviour of χ (or $|A_+|$ and $|A_-|$) is attributable to a 180° jump in the relative Langmuir-circulation–standing-wave phase when the cellular motion reverses. Finally, we observe that (4.10) constrains physically admissible solutions to the region of phase space bounded by the heteroclinic connections.

In figure 3, we plot $|E|$ (dark line), $|A|$ and $|B|$ (light lines) for two different sets of 'representative' initial conditions. Two time scales are evident: a high-frequency oscillation in the internal-wave amplitudes, associated with the reflections identified in Part 1, and a slower oscillation in the amplitudes of both the internal waves and the Langmuir circulation resulting from cell–wave energy exchanges. Figure 3(*a*) shows the interaction triggered by a resonant internal wave train propagating through a field of weak Langmuir cells. An immediate consequence is the generation of a reflected internal wave train. For longer times (up to $t \approx 40$), the cells are able to extract energy from the internal waves, leading to a five-fold increase in the amplitude of the Langmuir circulation. The initial conditions in figure 3(*b*) correspond to finite-amplitude Langmuir circulation above a relatively quiescent (but sharp) thermocline. As long as there is some disturbance energy initially in one of the resonant internal waves, the Langmuir cells will lose stability owing to energy transfer to those waves.

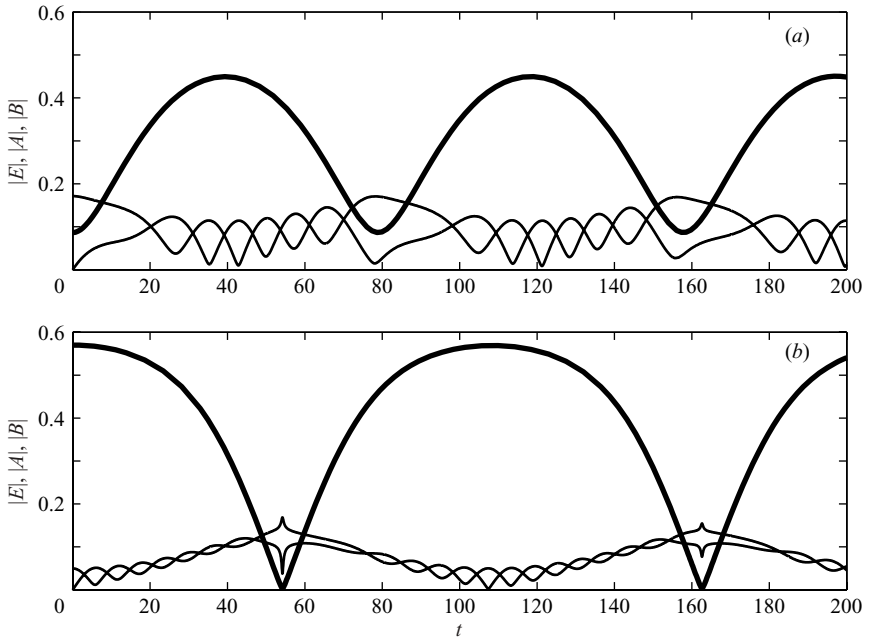

FIGURE 3. Nonlinear Langmuir-circulation–internal-wave oscillations: $|E|$ (dark line), $|A|$ and $|B|$ (light lines). Parameter values are the same as those used in figure 2. (*a*) Initial conditions chosen to simulate the effect of a single internal wave train incident upon a field of Langmuir cells; note the five-fold amplification of the Langmuir circulation for $t < 40$. (*b*) Initial conditions chosen to simulate steady Langmuir circulation above a sharp but relatively quiescent thermocline; the cells (temporarily) lose stability to a near standing-wave disturbance.

Note that the amplitudes of the counter-propagating waves remain nearly equal for the duration of the interaction, indicating that the Langmuir cells preferentially amplify a standing internal-wave disturbance.

The apparent 'spikes' in the internal-wave amplitudes which occur when $|E| \to 0$ result from the reconstruction of $|A|$ and $|B|$ from $|A_+|$ and $|A_-|$:

$$|A| = [|A_+|^2 + |A_-|^2 + 2|A_+||A_-|\cos(2\theta + \Phi_+ - \Phi_-)]^{1/2}, \tag{4.13}$$

$$|B| = [|A_+|^2 + |A_-|^2 - 2|A_+||A_-|\cos(2\theta + \Phi_+ - \Phi_-)]^{1/2}. \tag{4.14}$$

Consideration of (3.30) and (3.31) indicates that $|A_+|$ and $|A_-|$ vary rapidly (on the T-scale) in that limit, as shown in figure 4(*a*), so that the presumed separation between the τ- and T-scales vanishes. Figure 4(*b*) shows the evolution of the variable combinations $|A_+|^2 + |A_-|^2$ and $2|A_+||A_-|$ used in the reconstruction; note the spikes in the latter quantity, which occur as $|E| \to 0$. To properly relate the oscillatory internal-wave amplitudes $|A|$ and $|B|$ across the 'turning point' (where $|E| \to 0$), a small-$|E|$ analysis is required, which is beyond the scope of the present work. A cursory inspection of the non-uniform equations (3.2)–(3.4) does not suggest blow-up behaviour. This claim is further substantiated in the next section, where we investigate the limiting case of a Langmuir-circulation–standing-internal-wave interaction. Although E passes through zero, this interaction is properly described by the averaged equations (3.28), (3.30) and (3.31), since the τ-scale internal-wave

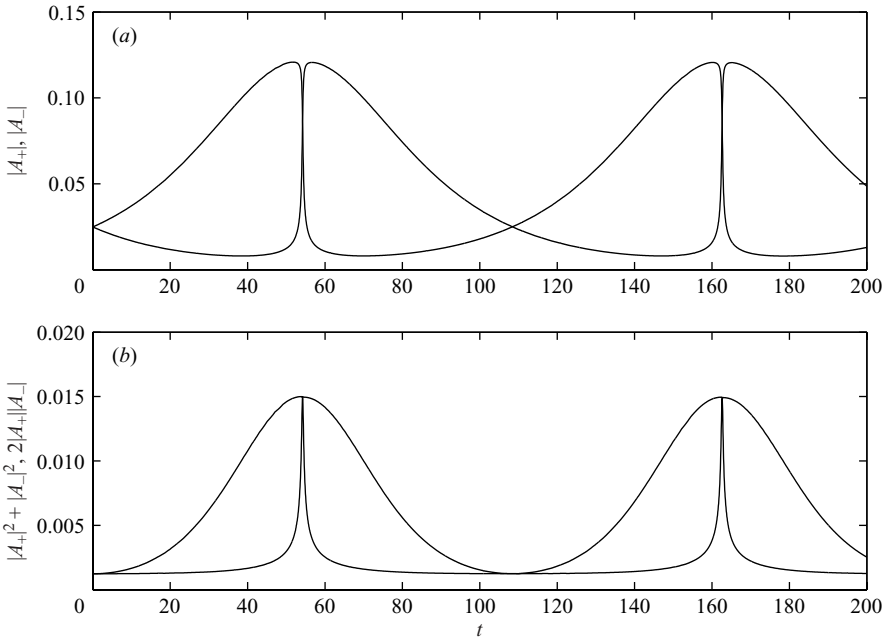

FIGURE 4. (*a*) Evolution of $|A_+|$ and $|A_-|$. (*b*) Evolution of $|A_+|^2 + |A_-|^2$ (smooth curve) and $2|A_+||A_-|$; the spikes exhibited in the latter variable combination occur as $|E| \to 0$. Parameters and initial conditions are the same as those used to generate figure 3(*b*).

reflections are absent for a pure standing-wave motion, i.e. $|A|$, $|B|$ and $|E|$ evolve only over the T-scale.

5. Langmuir-circulation–standing-internal-wave interaction

5.1. *Exact nonlinear solution*

The condition that the two counter-propagating waves superpose to form a standing wave is satisfied by requiring $|A| = |B|$. Thus, we express $B = \mathrm{e}^{\mathrm{i}\zeta} A^*$, which when combined with (3.21) and (3.22) requires

$$A_-^* \, \mathrm{e}^{\mathrm{i}\zeta} = -\frac{E}{|E|} A_-^* \quad \text{and} \quad A_+^* \, \mathrm{e}^{\mathrm{i}\zeta} = \frac{E}{|E|} A_+^*. \tag{5.1}$$

Conditions (5.1) can be satisfied only if $A_- = 0$ or $A_+ = 0$ or both. If $A_- = 0$ and $A_+ \neq 0$, $\zeta = \pi$ and $A = -B^*$ for $E < 0$, while for $E > 0$, $\zeta = 0$ and $A = B^*$. Conversely, if $A_+ = 0$ and $A_- \neq 0$, $\zeta = 0$ and $A = B^*$ for $E < 0$, and $\zeta = \pi$ and $A = -B^*$ for $E > 0$. Since χ changes sign for all physically admissible unsteady interactions (see figure 2), it is not possible for A_+ or A_- to equal zero for all time. Rather, the only possibility consistent with (5.1) is that $A_+ = 0$, $A_- \neq 0$ for $\chi < 0$ and $A_+ \neq 0$, $A_- = 0$ for $\chi > 0$. This requires that χ changes discontinuously (since $|A_+| = |A_-| = 0$ only for the steady saddle-node solutions $E^2 = C/r$), i.e. that E passes through zero (cf. (4.12)). Thus, $A = B^*$ or $A = -B^*$ throughout the lifetime of the interaction. In either case, an initial standing-wave disturbance persists as a standing wave only if it exhibits one of two possible phase relationships with the Langmuir cells (see figure 6 below).

We restrict attention to the $A = B^*$ scenario, since the $A = -B^*$ case can be recovered by translating the y-coordinate by $\pi/(2k)$. For $E < 0$, $A_+ = 0$ and $\chi = -\Gamma$, while for

$E > 0$, $A_- = 0$ and $\chi = \Gamma$. In both cases, $\Gamma = |A|^2 = |B|^2$ (since either A_+ or A_- is zero; cf. (4.13)–(4.14)), and the amplitude equations (4.11) and (4.12) can be written

$$\frac{\mathrm{d}E}{\mathrm{d}\mathscr{T}} = \Gamma, \tag{5.2}$$

$$\frac{\mathrm{d}\Gamma}{\mathrm{d}\mathscr{T}} = -2r\,E\Gamma. \tag{5.3}$$

According to (5.3), $\mathrm{d}\Gamma/\mathrm{d}\mathscr{T} = 0$ when E passes through zero, so $|A|$ and $|B|$ are stationary at that instant, i.e. the solution is physically well-behaved. Using (4.10) and (5.2) and imposing the 'initial' condition $E = 0$ at $\mathscr{T} = \mathscr{T}_m$, we obtain

$$E = |A_m|\, r^{-1/2} \tanh\left\{|A_m|\, r^{1/2}\,(\mathscr{T} - \mathscr{T}_m)\right\}, \tag{5.4}$$

where $|A_m|$ is the magnitude of the A wave at $\mathscr{T}_m$. Substituting (5.4) into (5.3) and integrating yields

$$|A| = |A_m| \operatorname{sech}\left\{|A_m|\, r^{1/2}\,(\mathscr{T} - \mathscr{T}_m)\right\}. \tag{5.5}$$

Thus, the amplitude of the Langmuir circulation increases monotonically from $-|A_m|r^{-1/2} = -(C/r)^{1/2}$ (since $C = |A_m|^2$) as $\mathscr{T} \to -\infty$ to $|A_m|r^{-1/2} = (C/r)^{1/2}$ as $\mathscr{T} \to \infty$, i.e. this solution corresponds to the heteroclinic orbit emanating from the lower saddle point in figure 2. When $A = -B^*$, E decreases monotonically from $|A_m|r^{-1/2}$ to $-|A_m|r^{-1/2}$, corresponding to the other heteroclinic connection. The amplitude of the standing wave tends to zero as $\mathscr{T} \to \pm\infty$ and reaches a maximum value at $\mathscr{T} = \mathscr{T}_m$, when E passes through zero.

In figure 5(*a*), we display the evolution of $|E|$ and $|A| = |B|$ for $|E|_{t=0} = 0.57$, $|A|_{t=0} = 0.035$ and $r = 0.042$, corresponding to $C = 0.015$. It is clear that the Langmuir circulation initially loses stability to the standing-wave disturbance but then recovers for $t > t_m$. Figure 5(*b*) reveals that the recovery is accompanied by a 180° phase shift in the position of the Langmuir-circulation surface-convergence zones. Since E changes sign, this phase shift is caused by a reversal in the orientation of the cellular motion.

5.2. *Physical mechanism*

The direction of energy transfer between the Langmuir circulation and standing internal wave is controlled by the phase relation between the modes. Figure 6 shows the two possibilities. In schematic (*a*) (case 1), the Langmuir circulation upwelling zones are aligned with the nodes of the standing wave. In schematic (*b*) (case 2), the downwelling zones are aligned with the standing-wave nodes. (For any other relative phase relation, the standing-wave disturbance will not persist.) Case 2 initial conditions were used to generate the solutions displayed in figure 5; the direction of energy transfer is from the cells to the standing wave in this case. When the cellular motion reverses, the case 1 scenario is realized. Energy is transferred from the wave to the cells, permitting the amplitude of the Langmuir circulation to recover. In both cases, it should be recalled that the standing wave undergoes very many oscillations before the amplitude of the wave or the cells changes appreciably (in accord with a weakly nonlinear interaction).

To gain insight into the interaction mechanism, we substituted the perturbation solutions obtained in Part 1 into expansions analogous to (3.1) to re-construct the linear Langmuir-circulation and standing-wave cross-wind velocity and displacement

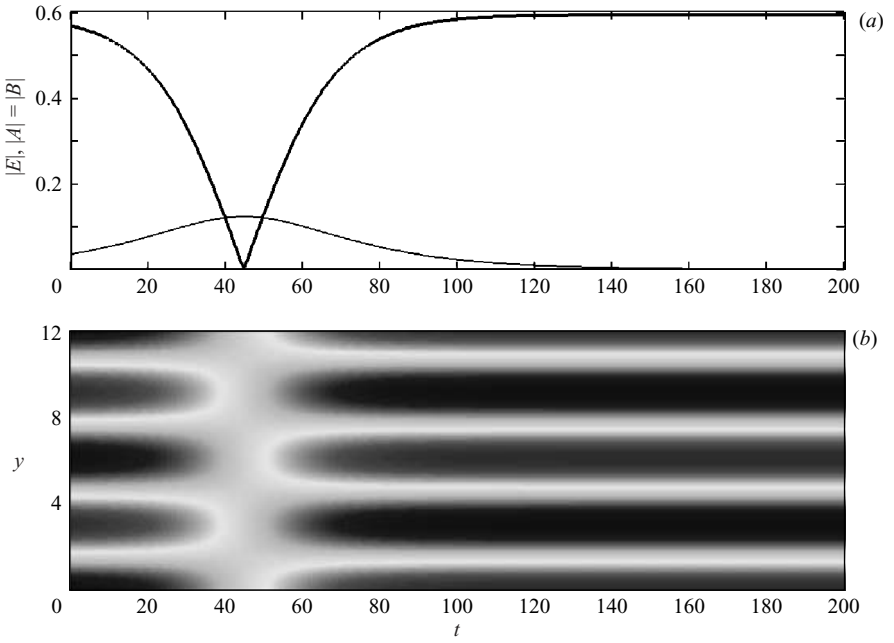

FIGURE 5. Nonlinear Langmuir-circulation–standing-wave interaction. (Parameter values given in text.) (*a*) Evolution of the magnitudes of the modal amplitudes, with the upper curve corresponding to the Langmuir circulation and the lower curve to the standing wave. (*b*) Spatio-temporal evolution of Langmuir-circulation surface-convergence field; time (t) is plotted on the horizontal axis and cross-wind distance (y) is plotted on the vertical axis. The evident 180° phase shift in the convergence zones is caused by a reversal in the orientation of the cellular motion.

fields:

$$v_{LC}(y,z,t) \sim k\frac{R_*S}{6}(4z^3+6z^2-1)\,E(t)\sin 2ky, \tag{5.6}$$

$$w_{LC}(y,z,t) \sim k^2\frac{R_*S}{3}(z-2z^3-z^4)\,E(t)\cos 2ky, \tag{5.7}$$

$$\eta_{LC}(y,t) \sim -\frac{S}{\gamma F}\,E(t)\cos 2ky, \tag{5.8}$$

and e.g. setting $\mathrm{Re}(B)=\mathrm{Re}(A)\equiv A_r$ and $\mathrm{Im}(B)=\mathrm{Im}(A)\equiv 0$ (recalling A and B actually represent $\tilde{A}$ and $\tilde{B}$) so that $A=B^*$,

$$\begin{aligned} v_{SW}(y,z,t) \sim{}& \left[\frac{8c}{R_*}-4k\frac{c(1+\gamma)}{R_*}\right]A_r(t)\sin ky\sin\Omega t \\ &-k\frac{R_*S}{30}(5-30z^2-20z^3)\,A_r(t)\sin ky\cos\Omega t, \end{aligned} \tag{5.9}$$

$$\begin{aligned} w_{SW}(y,z,t) \sim{}& -\left[k\frac{8c}{R_*}z-4k^2\frac{c(1+\gamma)}{R_*}z\right]A_r(t)\cos ky\sin\Omega t \\ &+k^2\frac{R_*S}{30}(5z-10z^3-5z^4)\,A_r(t)\cos ky\cos\Omega t, \end{aligned} \tag{5.10}$$

$$\eta_{SW}(y,t) \sim -\frac{8}{R_*}\,A_r(t)\cos ky\cos\Omega t, \tag{5.11}$$

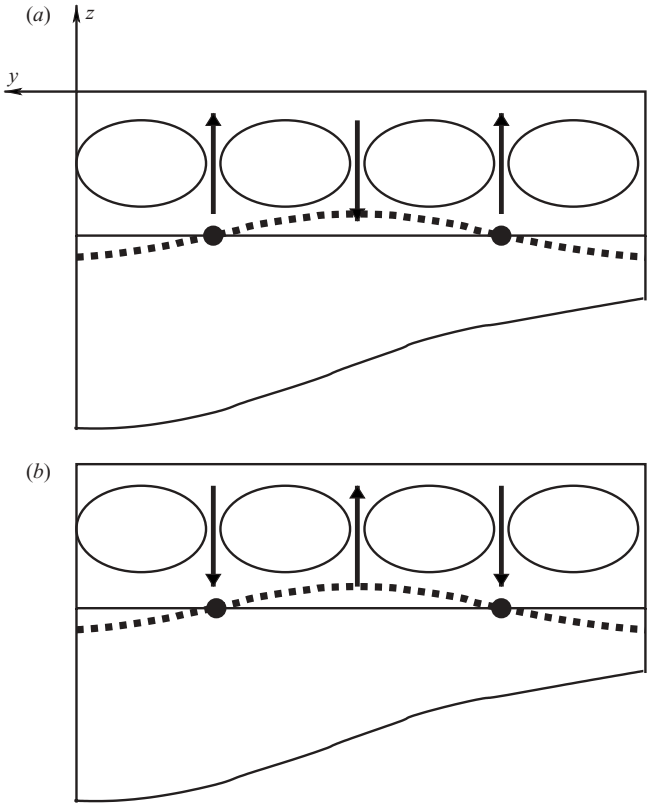

FIGURE 6. Sensitivity of Langmuir-circulation–standing-internal-wave energy transfers to the phase relation between the modes. In case 2 (*b*), the Langmuir-cell (LC) downwelling zones are aligned with the standing-wave (SW) nodes, and the cells lose energy to the wave. However, when the amplitude of the cells reaches zero, the orientation of the cellular motion and the direction of energy transfer reverse; the ensuing phase relation is shown in (*a*) (case 1).

where SW refers to standing wave, $\Omega \equiv \omega - k^2c(1+\gamma)/2$ and (5.9) and (5.10) have been corrected to account for the neglect of viscous internal-wave damping. These solutions are displayed in figure 7 at an instant when the standing-wave distortion of the thermocline is maximum and the amplitude of the Langmuir circulation is increasing (i.e. case 1). A striking feature is the cellular motion evident in the internal-wave velocity field. If S were zero, the cross-wind velocity field would vanish at this instant (cf. (5.9)–(5.10)), as might be anticipated for a standing-wave motion in a two-layer fluid. Instead, the CL vortex force succeeds in driving a transient cellular motion reminiscent of Langmuir circulation. Figure 8 contrasts the kinematics of traditional and vortex-force-modified standing waves over one cycle.

This transient vortex-force-induced flow field, which is strongest when the thermocline is maximally distorted every half-period of the standing-wave oscillation, is crucial to the transfer of energy between the standing wave and the Langmuir cells. To illustrate, consider the $v_{SW}\partial\eta_{SW}/\partial y$ nonlinearity in the kinematic interfacial condition (2.7), which accounts for the vertical velocity induced by the distortion of the interface. At the instant depicted in figure 7, the induced vertical velocity reaches a positive maximum at the nodes of the standing wave, thereby reinforcing

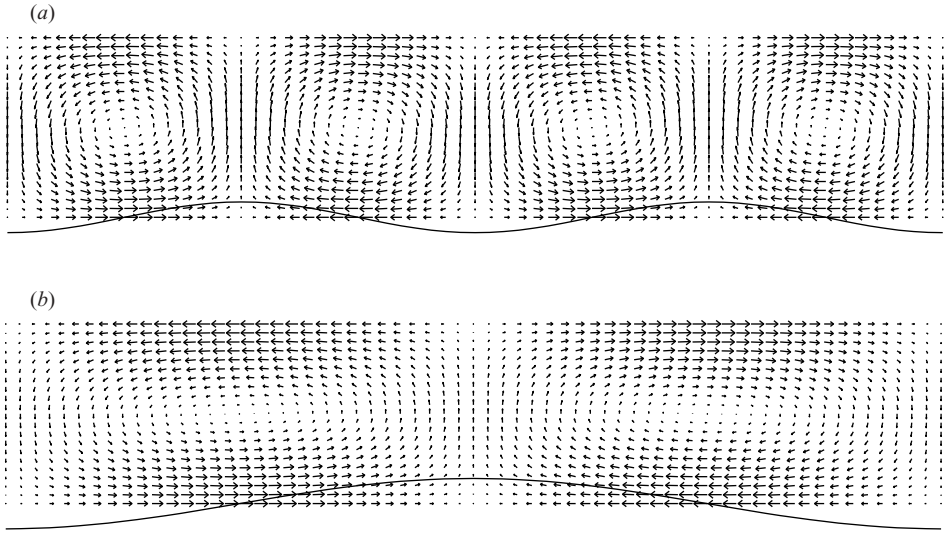

FIGURE 7. Snapshot of (*a*) the Langmuir-circulation and (*b*) standing-wave cross-wind velocity fields at an instant when the thermocline is maximally distorted by the standing internal wave. In each plot, the solid curve shows the associated deformation of the thermocline.

the Langmuir-cell upwelling zones, which are aligned with the nodes (i.e. the case 1 phase relation). One-half period later, the internal-wave-induced displacement of the thermocline is reversed but so, too, is the vortex-force-induced cellular motion (figure 8*f*). Thus, the reinforcement of the Langmuir-cell upwelling sites does not average to zero over a complete oscillation of the standing wave. Furthermore, the effect is comparably strong, since the internal wave spends the majority of each cycle in configurations involving significant distortion of the thermocline. Over many oscillations, this nonlinearity contributes to the uni-directional transfer of energy from the standing wave to the Langmuir circulation. Conversely, when the downwelling zones of the cells are aligned with the internal wave nodes (the case 2 phase relation), the upwelling induced at the nodes opposes the flow due to the Langmuir cells, causing them to transfer energy to the standing wave.

6. Discussion

Asymptotic analysis has been used to investigate the possibility for resonant nonlinear coupling between Langmuir circulation and counter-propagating internal waves in an idealized two-layer ocean model. Clearly, our rather stringent modelling assumptions – particularly, the restriction to two-dimensional long-wavelength weakly nonlinear dynamics – may limit the applicability of our results to actual Langmuir circulation. Nevertheless, we believe that the small-k asymptotic analysis presented here is useful. First, as mentioned in § 1, Cox (1997) has demonstrated that the long-wavelength approximation accurately captures linear Langmuir circulation dynamics even as $k_{LC} \to 1^{-}$. Next, under strongly supercritical conditions, a range of Langmuir circulation scales is excited; although cells with much larger horizontal than vertical scales may not be the most energetic (making the weakly nonlinear analysis more relevant), stability analyses indicate that they are likely to be present. Our analysis

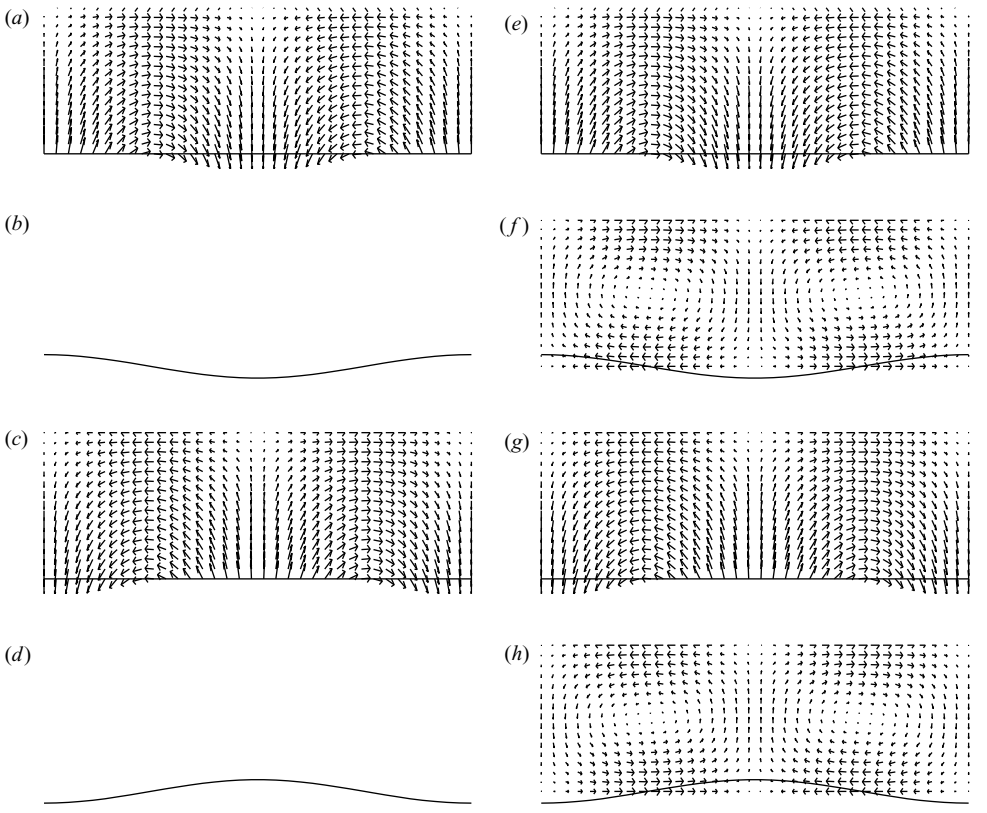

FIGURE 8. (*a–d*) Traditional and (*e–h*) CL vortex-force-modified standing waves.

suggests that these long-wavelength modes may be involved in the resonant interaction studied here. Finally, by formulating an analytically tractable model, we have found that the interaction depends crucially on the modification of the linear internal-wave dynamics by the CL vortex force. To assess whether this mechanism is sufficiently robust to occur in conditions different from those required for the formal validity of our asymptotic theory, full (non-hydrostatic) two-dimensional numerical simulations are being conducted; the results of this computational program will be reported elsewhere.

We briefly summarize our key results. In Part 1, we demonstrated that cross-wind propagating internal waves with wavenumber k will be reflected by wind-aligned Langmuir cells with wavenumber $2k$ over an $O(k^{-2})$ time scale. In this article, we have obtained a consistent asymptotic description of the interaction over an $O(k^{-3})$ time scale by using a WKBJ approximation to average over the comparatively high-frequency internal-wave reflections. This description admits only simple dynamics (i.e. nonlinear oscillations), at least when the cells and waves are modelled as linearly neutral modes. The long-time dynamics are controlled by the initial conditions or, equivalently, since all interactions exhibit instantaneous standing-wave behaviour, by the relative Langmuir-circulation–standing-wave phase. In contrast, the non-uniform resonant interaction equations admit quasi-periodic and transiently chaotic dynamics (Chini 1999).

Although simple, the long-time interaction dynamics – if realized – could influence the evolution of the mixed layer. For example, a (resonant) propagating internal wave incident upon a weak Langmuir-circulation field may 'spin up' the cells (figure 3*a*), possibly contributing to the maintenance of the mixed layer. Conversely, even if there is little energy initially in the resonant internal waves (figure 3*b*), as in the case of steady Langmuir circulation above a relatively quiescent but sharp thermocline, the cells may at least transiently lose stability to such disturbances. Our analysis suggests the following sequence of events. Langmuir cells preferentially amplify those standing-wave disturbances that have nodes aligned with the cell downwelling zones. The Langmuir circulation weakens, ultimately permitting the cellular motion to reverse. The cell upwelling zones are then aligned with the nodes of the standing internal wave, and the Langmuir circulation intensifies as energy is transferred from the wave. In general, the cells will not amplify a pure standing-wave disturbance; hence, the entire transient-instability process repeats. The Langmuir-circulation–standing-wave energy exchanges can be traced primarily to three nonlinearities in the conditions imposed at the thermocline: $v_{SW}\partial\eta_{SW}/\partial y$, $\eta_{SW}\partial^2 v_{SW}/\partial z^2$ and $\eta_{SW}\partial^2 u_{SW}/\partial z^2$. Each of these terms contributes to time-averaged energy transfers between the modes because the standing-wave cross-wind velocity field does not vanish when the thermocline is maximally distorted every half-period. Instead, the CL vortex force drives cellular motions at those instants.

The interaction period necessarily scales with the amplitudes of the cells and waves. If these are small, as assumed here, the interaction is weakly nonlinear; our estimates suggest that the time scale for the instability may be many hours. Of course, the lifetime of a Langmuir cell may be less than this, but fields of cells have been observed to persist for days under relatively steady forcing conditions (Farmer *et al.* 2001). The analysis presented here describes the time-averaged (downwind-averaged) behaviour of a Langmuir circulation field. The observations of Smith (1998) are interesting in this regard. Despite steady surface forcing, his data indicate 180° vacillations in the relative position of the Langmuir-cell surface convergence zones, consistent with a periodic reversal in the direction of the cellular motion. Smith speculated that the oscillations may have been caused by the dynamical influence of near-surface bubbles. In the light of our analysis, it seems possible that the periodic breakdown of the Langmuir circulation could have been caused by a resonant interaction with internal waves. Although the half-hour period of the vacillations is much less than the period of the nonlinear oscillations depicted, e.g. in figure 3(*b*), more realistic estimates of the Langmuir-circulation amplitude yield an oscillation time scale comparable to that observed by Smith. We hope that our results may be sufficiently interesting to prompt observational oceanographers to search for credible empirical evidence of Langmuir-circulation–internal-wave interactions.

G.P.C. is indebted to Stephen Cox (Nottingham University) for enlightening discussions on the asymptotic analysis described in this paper.

REFERENCES

Busse, F. H. & Riahi, N. 1980 Nonlinear convection in a layer with nearly insulating boundaries. *J. Fluid Mech.* **96**, 243–256.

Chapman, C. J. & Proctor, M. R. E. 1980 Nonlinear Rayleigh–Benard convection between poorly conducting boundaries. *J. Fluid Mech.* **101**, 759–782.

Chini, G. P. 1999 Resonant interaction of large-scale Langmuir circulation and thermoclinic internal waves. PhD thesis, Cornell University.

Chini, G. P. & Leibovich, S. 2003 Resonant Langmuir-circulation–internal-wave interaction. Part 1. Internal wave reflection. *J. Fluid Mech.* **495**, 35–55.

Colinet, P., Legros, J. C. & Velarde, M. G. 2001 *Nonlinear Dynamics of Surface-Tension-Driven Instabilities*. Berlin: Wiley-VCH.

Cox, S. M. 1997 Onset of Langmuir circulation when shear flow and Stokes drift are not parallel. *Fluid Dyn. Res.* **19**, 149–167.

Cox, S. M. & Leibovich, S. 1993 Langmuir circulations in a surface layer bounded by a strong thermocline. *J. Phys. Oceanogr.* **23**, 1330–1345.

Cox, S. M. & Leibovich, S. 1994 Large-scale Langmuir circulation and double-diffusive convection: Evolution equations and flow transitions. *J. Fluid Mech.* **276**, 189–210.

Cox, S. M. & Leibovich, S. 1997 Large-scale three-dimensional Langmuir circulation. *Phys. Fluids* **9**, 2851–2863.

Craik, A. D. D. & Leibovich, S. 1976 A rational model for Langmuir circulations. *J. Fluid Mech.* **73**, 401–426.

Farmer, D., Vagle, S. & Li, M. 2001 Bubble and temperature fields in Langmuir circulation. In *Fluid Mechanics and the Environment: Dynamical Approaches* (ed. J. L. Lumley). Springer.

Garcia-Ybarra, P. L., Castillo, J. L. & Velarde, M. G. 1987 Benard–Marangoni convection with a deformable interface and poorly conducting boundaries. *Phys. Fluids* **30**, 2655–2661.

Gertsberg, V. L. & Sivashinsky, G. I. 1981 Large cells in nonlinear Rayleigh–Benard convection. *Prog. Theor. Phys.* **66**, 1219–1229.

Golovin, A. A., Nepomnyashchy & Pismen, L. M. 1995 Pattern formation in large-scale Marangoni convection with deformable interface. *Physica* D **81**, 117–147.

Hefer, D. & Pismen, L. M. 1987 Long-scale thermodiffusional convection. *Phys. Fluids* **30**, 2684–2694.

Hinch, E. J. 1991 *Perturbation Methods*. Cambridge University Press.

Johnson, D. & Narayanan, R. 1996 Experimental observation of dynamic mode switching in interfacial-tension-driven convection near a codimension-two point. *Phys. Rev.* E **54**, 3102–3104.

Knobloch, E. 1990 Pattern selection in long-wavelength convection. *Physica* D **41**, 450–479.

Knobloch, E. & De Luca, J. 1990 Amplitude equations for travelling wave convection. *Nonlinearity* **3**, 975–980.

Knobloch, E. & Gibbon, J. D. 1991 Coupled NLS equations for counter propagating waves in systems with reflection symmetry. *Phys. Lett.* A **154**, 353–356.

Leibovich, S. 1977 On the evolution of the system of wind drift currents and Langmuir circulations in the ocean. Part 1. Theory and averaged current. *J. Fluid Mech.* **79**, 715–743.

Leibovich, S. 1983 The form and dynamics of Langmuir circulations. *Annu. Rev. Fluid Mech.* **15**, 391–427.

Lindzen, R. S. 2003 The interaction of waves and convection in the tropics. *J. Atmos. Sci.* **60**, 3009–3020.

Majda, A. 2000 *Introduction to PDEs and Waves for the Atmosphere and Ocean*. American Mathematical Society.

McWilliams, J. C., Sullivan, P. P. & Moeng, C. 1997 Langmuir turbulence in the ocean. *J. Fluid Mech.* **334**, 1–30.

Mei, C. C. 1985 Resonant reflection of surface water waves by periodic sandbars. *J. Fluid Mech.* **152**, 315–335.

Pavithran, S. & Redekopp, L. G. 1994 The coupling of gravity waves and convection: Amplitude equations and planform selection. *Stud. Appl. Math.* **93**, 209–250.

Phillips, O. M. 1977 *The Dynamics of the Upper Ocean*, 2nd edn. Cambridge University Press.

Pierce, R. D. & Knobloch, E. 1994 On the modulational stability of traveling and standing water waves. *Phys. Fluids* **6**, 1177–1190.

Pismen, L. M. 1988 Selection of long-scale oscillatory convective patterns. *Phys. Rev.* A **38**, 2564–2572.

Proctor, M. K. & Jones, C. 1988 The interaction of two spatially resonant patterns in thermal convection 1: exact 1:2 resonance. *J. Fluid Mech.* **188**, 301–335.

Sivashinsky, G. I. 1982 Large cells in nonlinear Marangoni convection. *Physica* D **4**, 227–235.

Sivashinsky, G. I. 1983 On cellular instability in the solidification of a dilute binary alloy. *Physica* **8**, 243–248.

Smith, J. 1998 Evolution of Langmuir circulation during a storm. *J. Geophys. Res.* **103** (C6), 12649–12668.

Thorpe, S. A. 1997 Interactions between internal waves and boundary layer vortices. *J. Phys. Oceanogr*. **27**, 62–71.

Thorpe, S. A. 2004 Langmuir circulation. *Annu. Rev. Fluid Mech.* **36**, 55–79.